Section 2

Data sets, diagnostic and dynamical investigations, statistical post-processing, reanalysis, and associated studies.

SPATIOTEMPORAL DISTRIBUTIONS OF GLOBAL TRENDS OF WATER VAPOUR AMOUNT IN THE 0-30 KM ATMOSPHERIC LAYER

O.A. Aldukhov and I.V. Chernykh
Russian Institute of Hydrometeorological Information – World Data Center, Obninsk, Russia, E-mail: aoa@meteo.ru, civ@meteo.ru

Introduction

Water vapour is one of greenhouse gases. The knowledge about long-term changes in water vapour amount (VA) distributions in the atmosphere based on hourly values is necessary in studying global climate change. The paper presents the series of the 1-st and 2-nd order trends [1] of water vapour amount at standard heights in the 0-30-km atmospheric layer over sea level for different months, seasons and the year as a whole.

Data and methods

The CARDS global aerological dataset [2] updated by current data [3] for the period 1964–2018 was used in this research. The computations are based on the dataset from 770 stations with relatively homogeneous observations. The necessary condition for including a station in this study was 15-year observations for the full observation period including 2018.

The Akima cubic spline interpolation method was used to compute VA values and their standard deviations (σ_{VA}) in the 0–30-km layer above sea level on the basis of standard pressure levels and specific points of vertical profiles.

The trends were calculated for each station by using the classic least squares method. The values obtained for all stations were averaged considering the area of the station influence. The anomalies were calculated with respect to the long-term means for the full period 1964–2018.

Results

The Figure shows spatiotemporal distributions of long-term monthly means and standard deviations (σ_{VA}), the 1-st and 2-nd order trends for anomalies of water vapour amount and σ_{VA} in the 0–30-km atmospheric layer for different months, seasons and the whole year.

The annual changes of the long-term monthly means in the 0–30-km layer range from 4.23 to 27.11 kg/m^2 for VA. The annual changes of the 1-st order trends of the long-term monthly means anomalies in the 0–30-km layer range from -0.040 to 0.143 kg/m^2/decade for VA. The global water vapour amount in this layer increases mainly at 0–3 km for all months, while at 0–30 km it increases from June to September.

The annual changes in standard deviations σ_{VA} range from 3.05 to 16.69 kg/m^2. The 1-st order trends of σ_{VA} are negative for all months in the entire 0–4-km layer and throughout the 0–30-km layer from July to September. The most intense decrease of σ_{VA} is detected at 27–29 km in winter and autumn. The most intense increase of σ_{VA} (with significance of more than 95%) is detected in the entire 9–13-km layer for February and March. Significant increase of σ_{VA} is detected throughout the 0–2-km layer for all the months.

The 2-nd order trends for VA are positive for all months in the entire 0–30-km layer, which implies the acceleration of changes for VA with the year 2018 approaching. The annual changes in the 2-nd order trends of the long-term monthly means anomalies in the 0–30-km layer range from -0.018 to 0.257 kg/m^2/decade^2 for VA. The highest positive accelerations of changes for VA were detected at 8-26 km for winter and autumn and at 6-26 km, for spring.

The 2-nd order trends of standard deviations σ_{VA} are positive in the 8-30-km layer for all the months. The annual changes in the 2-nd order trends of standard deviations σ_{VA} in the 0–30-km layer range from -0.002 to 0.163 kg/m^2/decade^2. The highest positive accelerations of changes in σ_{VA} were detected at 18–26 km for spring.

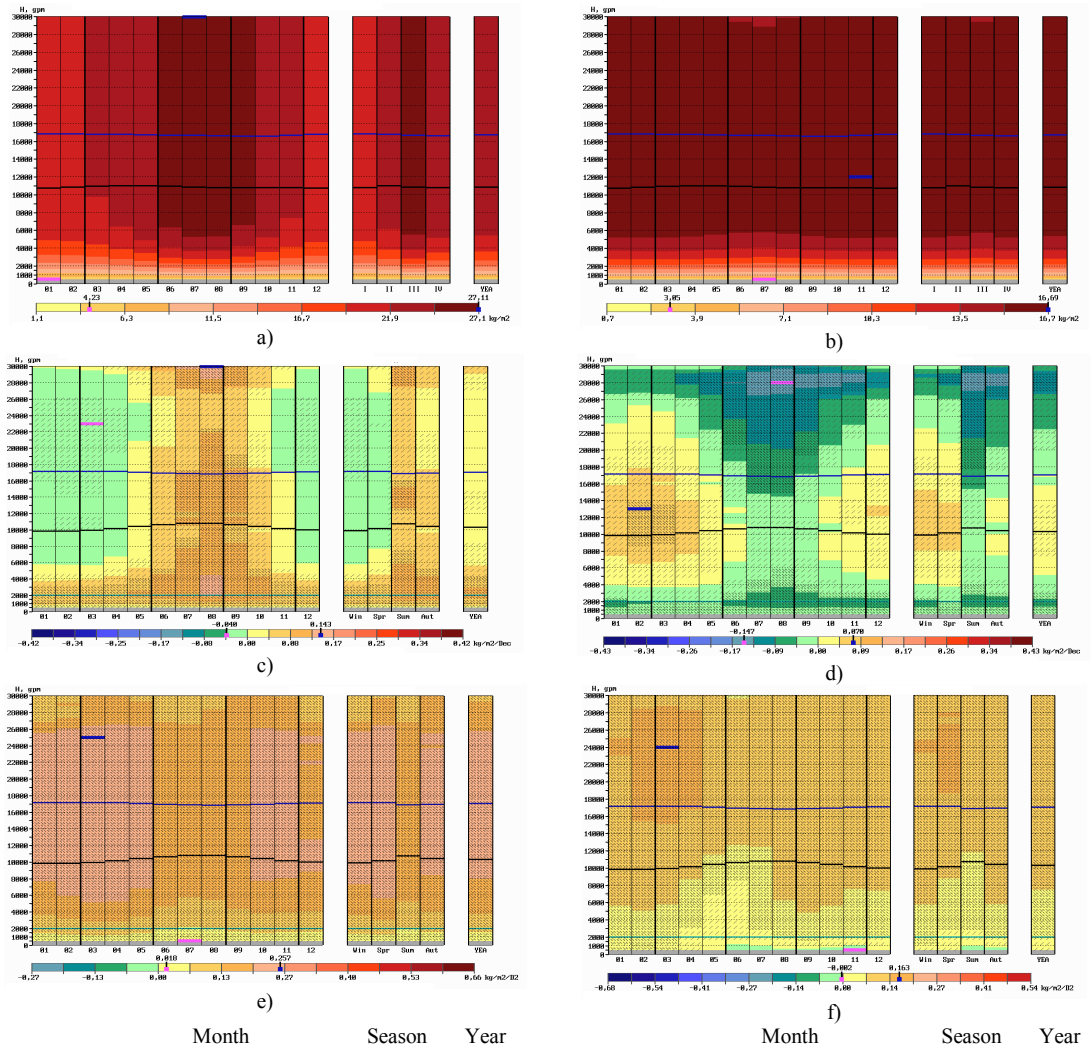

Figure. Long-term means (a), first-order trends of anomalies of long-term means for VA (c, kg/m^2/decade), second-order trends of anomalies of long-term means for VA (e, kg/m^2/decade^2), and standard deviations σ_{VA} (b), first-order (d) and second-order (f) trends of σ_{VA} in the 0–30-km atmospheric layer for the year as a whole, for each month and season. Blue and pink segments correspond to maximum and minimum values. The global statistics for months and seasons were subject to twofold smoothing. Three–points smoothing was used. Trends with significance of not less than 50% are marked by the sloping line segments and those with significance of not less than 95% – by lattice. Grey color marks areas with insufficient data for calculations. 1964–2018.

Conclusions

Spatiotemporal distributions of the linear trends of water vapour amount anomalies are not uniform in the 0–30-km atmospheric layer above sea level. The water vapour amount increases mainly in the entire 0–3-km layer for all the months and throughout the 0–30-km layer from June to September.

References

1. Aldukhov O.A., Chernykh I.V. First and second-order trends of air temperature at the surface level from global radiosonde data // Research activities in Earth system modelling. Working Group on Numerical Experimentation. Report No. 50. WCRP Report No.12/2020. Ed. E. Astakhova, July 2020, WMO, Geneva. Research Activities in Earth System Modelling WGNE Blue Book 2020), http://bluebook.meteoinfo.ru/, 2020, p. 2-03-2-04
2. Eskridge R.E., et. al. A comprehensive aerological reference dataset (CARDS): rough and systematic errors // Bull. Amer. Meteor. Soc. 1995. **76.** 1759-1775.
3. Rudenkova T.V. Format for archiving of the current aerological data, received from GTS for PC // Proc. RIHMI-WDC, 2010, N 174, p. 41–63.

FIRST AND SECOND-ORDER TRENDS OF WIND SPEED IN THE 0-30 KM ATMOSPHERIC LAYER FROM GLOBAL AEROLOGICAL DATASETS

O. A. Aldukhov and I. V. Chernykh
Russian Institute of Hydrometeorological Information – Word Data Center, Obninsk, Russia,
E-mail: aoa@meteo.ru, civ@meteo.ru

Introduction

The knowledge about long-term changes in wind speed (S) distributions in the atmosphere obtained from hourly values is necessary to study global climate change and to solve many practical problems. The paper presents the series of the 1-st and 2-nd order trends [1] of wind speed at standard heights in the 0–30-km atmospheric layer over sea level for the year as a whole, for different months and seasons.

Data and methods

Results of radiosounding observations from the CARDS global aerological dataset [2] that were updated by current data from RIHMI-WDC [3] for the period 1964–2018 were used in this study. The calculations are based on the dataset from 770 stations with relatively homogeneous observations. The necessary condition for including a station in the research was 15-year observations for the full observation period including 2018.

The Akima cubic spline interpolation method was used to calculate S values and their standard deviations (σ_S) in the 0–30-km layer above sea level on the basis of standard pressure levels and specific points of vertical profiles. The trends were computed for each station by using the least squares method. The anomalies were calculated with respect to the corresponding long-term means for the period 1964–2018. The values obtained for all the stations were averaged taking into account the area of the station influence.

Results

The Figure shows that the spatiotemporal distributions of the 1-st order trends (classical linear trends) for anomalies and standard deviations of wind speed are nonuniform in the 0–30-km atmospheric layer above sea level.

The annual changes in the long-term monthly means of the wind speed S in the 0–30-km layer range from 4.26 to 23.24 m/s. The annual changes of the 1-st order trends of the long-term monthly means anomalies in the 0–30-km layer range from -0.034 to 0.256 m/s per decade for S. The global wind speed in this layer mainly increases at 0–1 km and at 15–19 km for all months, while at 28–30 km it increases in May, November and December.

The annual changes in standard deviations σ_S of wind speed range from 3.26 to 16.53 m/s. The 1-st order trends of σ_S are negative for all months in the entire 5–12-km layer and positive for all months throughout the 14–30-km layer. The most intense decrease of σ_S (with significance of more than 95%) is detected at 3–9 km in winter and at 5–7 km for spring and autumn. The most intense increase of σ_S (with significance of more than 95%) is detected in the entire 18–30-km layer for summer and autumn. Significant increase in σ_S is detected throughout the 0–1-km layer for spring, summer and autumn

The 2-nd order trends for S are mostly positive, which implies the acceleration of changes for S with the year 2018 approaching. The annual changes in the 2-nd order trends of the long-term monthly means anomalies in the 0–30-km layer range from -0.085 to 0.405 m/s per decade^2 for S. The highest positive accelerations of changes for S were detected at 20–24 km in summer and autumn.

The 2-nd order trends of standard deviations σ_S are positive in the 0–17-km layer for winter and spring, in the 0–30-km layer, for summer, and in the 0–22-km and 28–30-km layers, for

autumn. The annual changes in the 2-nd order trends of standard deviations σ_S in the 0–30-km layer range from -0.155 to 0.294 m/s per decade^2.

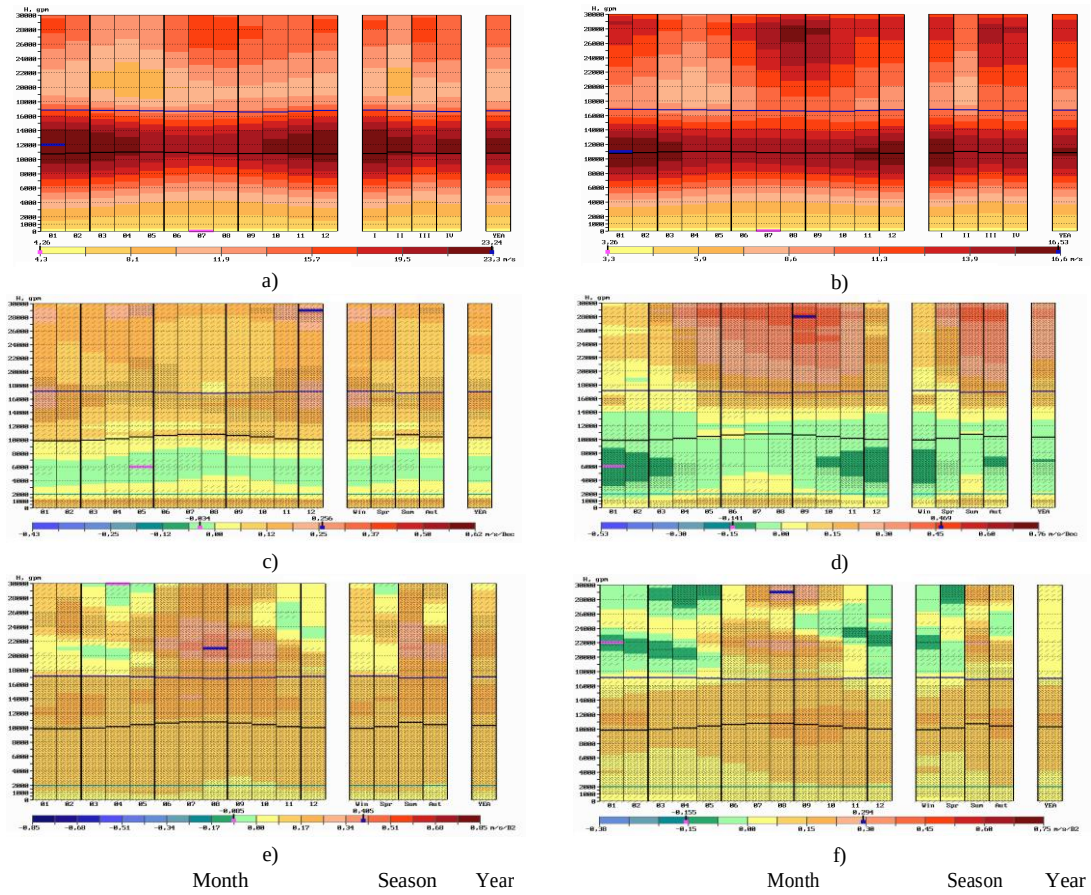

Figure. Long-term means (a), first-order trends of anomalies of long-term means for S (c, m/s/decade), second-order trends of anomalies of long-term means for S (c, m/s/decade^2), and standard deviations (b), first-order (d) and second-order (f) trends of standard deviations σ_S in the 0–30-km atmospheric layer for each month, season and the year as a whole. The global statistics for months and seasons were subject to twofold smoothing. Three–points smoothing was used. Trends with significance of not less than 50% are marked by the sloping line segments and those with significance of not less than 95% – by lattice. Blue and pink segments correspond to maximum and minimum values. 1964–2018.

Conclusions

Spatiotemporal distributions of the linear trends of wind speed anomalies are not uniform in the 0–30-km atmospheric layer above sea level. The wind speed increases mainly at the 0–1-km and at 15–19-km heights for all months, while at 28–30-km it increases in May, November and December.

References

1. Aldukhov O.A., Chernykh I.V. First and second-order trends of air temperature at the surface level from global radiosonde data // Research activities in Earth system modelling. Working Group on Numerical Experimentation. Report No. 50. WCRP Report No.12/2020. Ed. E. Astakhova, July 2020, WMO, Geneva. pp. 2-03-2-04. http://bluebook.meteoinfo.ru/uploads/2020/docs/02_Aldukhov_Oleg_GlobalTemperatureTrends.pdf
2. Eskridge R.E., et. al. A comprehensive aerological reference dataset (CARDS): rough and systematic errors // Bull. Amer. Meteor. Soc. 1995. **76.** 1759-1775.
3. Rudenkova T.V. Format for archiving of the current aerological data, received from GTS for PC // Proc. RIHMI-WDC, 2010, N 174, p. 41–63.

TRENDS OF THE NUMBER OF CLOUD LAYERS FROM GLOBAL RADIOSOUNDING DATA

I.V. Chernykh and O.A. Aldukhov
Russian Institute of Hydrometeorological Information – World Data Center, Obninsk, Russia,
E-mail: civ@meteo.ru, aoa@meteo.ru

Introduction

Estimates of the cloud layer number are useful for studying the atmospheric vertical structure and climatic changes, and for assessing propagation conditions of electromagnetic waves. Different aspects of research on the cloud layer number were discussed in [1–4]. The paper presents global long-term estimates of the number of reconstructed cloud layers with the cloud amount of 0–20, 20–60, 60–80, 80–100, 0–100% and trends of their anomalies. Calculations were conducted for the atmospheric layers 0–2, 2–6, 6–10 and 0–10 km above the surface level. Means and trends were found for each month, season and the year as a whole.

Data and methods

To determine cloud boundaries and cloud amount [5], we used CE-method and CARDS global dataset [6] supplemented by current data from AROCTAC dataset [7] for the 1964-2018 period. To compute the statistics, only observations including both temperature and humidity data from the surface to the 10-km height were applied. We did not consider cloud layers for which the CE-method gave thickness less than 50 m. The existence of several cloud layers with different cloud amounts was allowed.

Results

The Table presents global annual mean values and trends of anomalies of the cloud layer number with regard to the cloud amount gradation, as well as ranges of annual variations in monthly means and trends of their anomalies for the atmospheric layer of 0–10 km. The mean numbers of cloud layers with cloud amounts 0–100, 0–20 and 80–100% and the corresponding trends estimated for atmospheric layers 0–2, 2–6, 6–10, 0–10 km over the Globe are shown in the Figure for months, seasons and the year as a whole. The trends with significance of not less than 50% are marked by a square and those with significance of not less than 95% – by a square with a cross.

The trends were estimated for each station by using the least squares method. The anomalies were calculated with respect to the corresponding long-term mean values for the period 1964–2018. The values obtained for all stations were averaged taking into account the area of the station influence. The global statistics for months and seasons were subject to twofold smoothing. The three-points smoothing was used.

Table.

The global annual mean values and trends of anomalies of cloud layer number with taking into account the cloud amount gradation and intra-annual variations ranges (Δ) of monthly averaged values and trends of their anomalies for the atmospheric layer 0–10 km over the surface level.

Cloud coverage, %	Mean	Trends	Δ_{mean}	Δ_{trends}	Number of soundings, millions
0–20	4,2	0,023	4,25–4,36	0,021–0,026	15,4
20–60	1,5	0,004	1,51–1,52	0,003–0,005	7,7
60–80	1,2	0,003	1,19–1,20	0,003	4,1
80–100	2,8	0,017	2,67–2,88	0,016–0,019	12,3
0–100	6,62	0,036	6,59–6,65	0,033–0,038	17,9

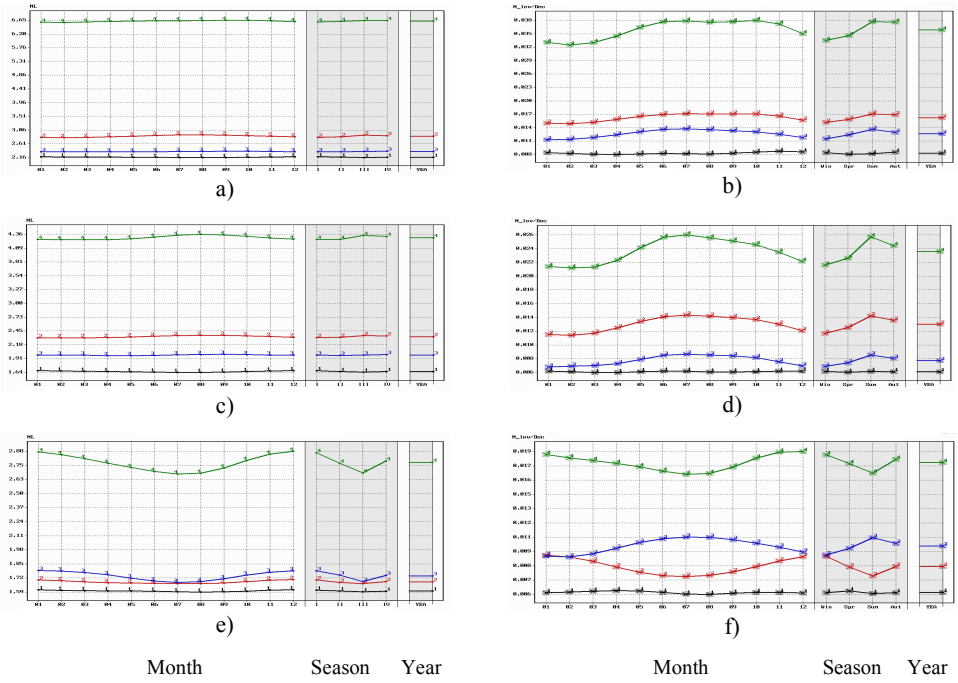

Figure. Global long-term means (a, c, e) and trends of their anomalies (b, d, f; n per decade) of the number (n) of cloud layers with regard to the cloud amount gradation for different atmospheric layers for each month, season and year. Black lines – for 0–2 km, red lines – 2–6 km, blue lines – 6–10 km, green lines – 0–10 km. (a, b) – 0–100%, (c, d) – 0–20%, (e, f) – 80–100% cloud coverage. 1964–2018.

Conclusions

The results show that the mean number of cloud layer and the trends of their anomalies depend on the cloud amount gradation. Their values for the gradations 0–20 and 80–100% are several times higher than those for the gradations 20–60, 60–80%.

Long-term monthly (seasonal) means of the number of cloud layers with the fixed cloud amount gradation differ little for each atmospheric layer considered in this paper.

The minimums of trends for cloud layers with cloud coverage 0–100% and 0–20% in the atmospheric layers 0–10, 2–6 and 6–10 km are detected in winter and the maximum – in summer. The cloud layer number increases in the 2–6-km atmospheric layer more than in the 6–10-km layer for all months and seasons.

The minimums of trends for cloud layers with cloud coverage 80–100% in the atmospheric layers 0–10 and 2–6 km are detected in summer and the maximums – in winter, while in the 6–10-km atmospheric layer, on the contrary, maximums – in summer and minimums – in winter.

References

1. Chernykh I.V., Aldukhov O.A. Estimating the Number of Cloud Layers through Radiosonde Data from Russian Aerological Stations for 1964– 2014 // Russian Meteorology and Hydrology, 2018, Vol. 43, No. 3, pp. 152–160.

2. Chernykh I.V., Aldukhov O.A. Long-term Estimates of the Number of Cloud Layers from Radiosonde Data for 1964–2017 in Different Latitudinal Zones // Russian Meteorology and Hydrology, 2020, Vol. 45, No. 4, pp. 227–238.

3. Chernykh I.V., Aldukhov O.A. Long-term space-time changes in the number of cloud layers reconstructed from radiosonde observations for Russian stations // Proceedings of RIHMI-WDC. 2020. N 187. P. 35–60.

4. Chernykh I.V., Alduchov O.A., Eskridge R.E. Reply to comments of D.J. Seidel and I. Durre on “Trends in low and high cloud boundaries and Errors in height determination of cloud boundaries” // Bull. Amer. Met. Society. 2003. Vol. 84, No. 2. P.241-247.

5. Chernykh I.V., Eskridge R.E. Determination of cloud amount and level from radiosonde soundings // J. Appl. Meteorol., 1996, vol. 35, pp. 1362–1369.

6. Eskridge R.E., Alduchov O.A., Chernykh I.V., Zhai P., Polansky A.C., Doty S.R. A comprehensive aerological reference dataset (CARDS): rough and systematic errors // Bull. Amer. Meteor. Soc. 1995. **76.** 1759–1775.

7. Rudenkova T.V. Format for archiving of the current aerological data, received from GTS for PC // Proc. RIHMI-WDC, 2010, N 174, p. 41–63.

A distance correlation ratio of predictable components

Rick Danielson (rickedanielson@gmail.com)
Fisheries and Oceans Canada, Halifax, Nova Scotia

Introduction

The ratio of predictable components (RPC) is a useful metric of forecast skill (Kumar et al. 2014; Eade et al. 2014), although it begs the question of whether one should expect an ensemble mean to covary more with observations than with its own ensemble members. An implicit assumption is that the forecast model is independent of observations, but even if the forecast model is not assimilative, there remains the possibility that errors are correlated, or in other words, that the observation and forecast model *measures* [in the context of a simple *measurement model* (Siegert et al. 2016)] are still not independent. A new correlation method has been developed by Székely et al. (2007) and Székely and Rizzo (2009) that allows this statistical independence assumption to be tested. We compare the two RPC values for a single raw ensemble simulation using the Lorenz 1963 modelling framework of Mayer et al. (2021).

Results

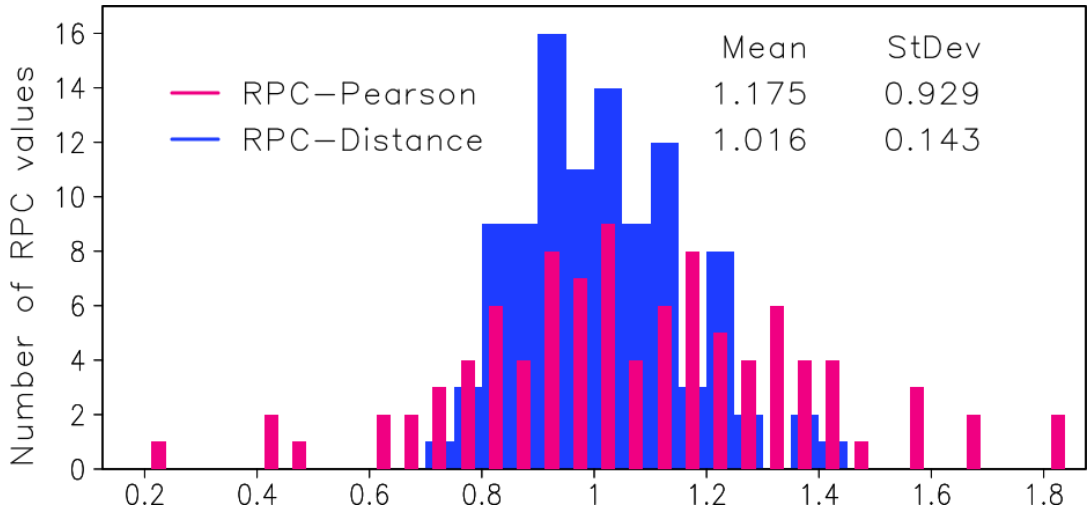

Figure 1: Distributions of the ratio of predictable components (RPC) for 100 40-member ensemble hindcasts of the Lorenz model (Mayer et al. 2021), where RPC is computed as a ratio of (red) Pearson correlations (Scaife and Smith 2018) and (blue) distance correlations (Székely et al. 2007; Székely and Rizzo 2009). The bin interval is 0.05 and the mean and standard deviation of the two distributions are included.

It is convenient to calculate a distance correlation RPC without the added concern of timeseries autocorrelation. Thus, instead of the monthly and seasonally averaged timeseries that is the focus of Mayer et al. (2021), we start with one of their raw ensemble simulations. For each of 100 different initial conditions on the Lorenz attractor, a noisy observational simulation and a 40-member ensemble is used to calculate RPC using either a ratio of Pearson or distance correlations (the RPC numerator is the correlation of observations with ensemble-mean, and the denominator is the average correlation over all ensemble members with the mean, excluding that member). In order to avoid autocorrelation, 20 samples at 100 time intervals are taken from each 2001-unit perturbed raw timeseries.

Figure 1 shows one of the underconfident (i.e., large initial spread) ensemble experiments of Mayer et al. (2021), which yields a mean RPC (Pearson) of greater than one and a large RPC standard deviation as well. Interestingly, the RPC (distance correlation) has a mean value closer to one, and hence, is more consistent with expectations (Kumar et al. 2014; Eade et al. 2014). The RPC variance is also much reduced.

Summary

It may be difficult to define predictability, and thus any *linear* measure of it, but perhaps a distance correlation RPC is also a viable diagnostic of forecast model skill. The physical basis for assuming that measures are independent is sound, although measurement models themselves are typically simple, and may implicitly impose a dependence. Strictly speaking, we do not consider a forecast ensemble that is marginally calibrated (Siegert et al. 2016), but it seems notable that under this assumption, RPC is approximately β^{-1} (i.e., inverse of the multiplicative parameter of linear agreement between model and observations). However, it is difficult to anticipate a value of β between the limits of ordinary and reverse linear regression. For a given value of distance correlation between 0 and 1, it seems that any value of β is possible (Edelmann et al. 2021).

Acknowledgements

M. Rizzo and G. Szekely are thanked for providing the distance correlation R package (energy). B. Mayer is thanked for providing the Lorenz model framework (https://doi.org/10.5281/zenodo.4418958), and J. Mecking is thanked for drawing attention to the RPC.

References

Eade, R., D. Smith, A. A. Scaife, E. Wallace, N. Dunstone, L. Hermanson, and N. Robinson, 2014: Do seasonal-to-decadal climate predictions underestimate the predictability of the real world? *Geophys. Res. Lett.*, **41**, 5620–5628, doi:10.1002/2014GL061146.

Edelmann, D., T. F. Móri, and G. J. Székely, 2021: On relationships between the Pearson and the distance correlation coefficients. *Stat. Prob. Lett.*, **169**, 1–6, doi:10.1016/j.spl.2020.108960.

Kumar, A., P. Peng, and M. Chen, 2014: Is there a relationship between potential and actual skill? *Mon. Wea. Rev.*, **142**, 2220–2227, doi:10.1175/MWR–D–13–00287.1.

Mayer, B., A. Düsterhus, and J. Baehr, 2021: When does the Lorenz 1963 Model exhibit the signal-to-noise paradox? *Geophys. Res. Lett.*, **48**, 1–10, doi:10.1029/2020GL089283.

Scaife, A. A., and D. Smith, 2018: A signal-to-noise paradox in climate science. *npj Clim. Atmos. Sci.*, **1**, 1–8, doi:10.1038/s41612–018–0038–4.

Siegert, S., D. B. Stephenson, P. G. Sansom, A. A. Scaife, R. Eade, and A. Arribas, 2016: A Bayesian framework for verification and recalibration of ensemble forecasts: How uncertain is NAO predictability? **29**, 995–1012, doi:10.1175/JCLI–D–15–0196.1.

Székely, G. J., and M. L. Rizzo, 2009: Brownian distance covariance. *Annals of Applied Statistics*, **3**, 1236–1265, doi:10.1214/09AOAS312.

Székely, G. J., M. L. Rizzo, and N. K. Bakirov, 2007: Measuring and testing dependence by correlation of distances. *Annals of Statistics*, **35**, 2769–2794, doi:10.1214/009053607000000505.

Some aspects of the weak rainfall spells of the Indian summer monsoon 2018

Sujata K. Mandke [1, *]
[1] Indian Institute of Tropical Meteorology, Ministry of Earth Sciences, India
*amin@tropmet.res.in

1. Introduction

During summer monsoon season from June to September (JJAS), rainfall over Indian region exhibits large intra-seasonal fluctuations between active and weak spells. Intense weak/dry spells of rainfall are referred to as breaks during the peak monsoon months of July-August (Ramamurthy, 1969). Despite extensive research on breaks in Indian summer monsoon (ISM) (Krishnan et al. 2000, Gadgil and Joseph, 2003, Rajeevan et al. 2010), the links of monsoon variability over Indian region to that over the Indian ocean and the Pacific are not adequately understood. This topic is addressed in the present study for weak/break rainfall phases during JJAS 2018. All weak/lull/break spells are referred as weak spells.

2. Data

(i)Daily merged satellite gauge rainfall data (0.25°x0.25°) (Mitra et al. 2009) (https://www.imdpune.gov.in/Seasons/Temperature/gpm/Rain_Download.html) (ii) Daily un-interpolated Outgoing Longwave Radiation (OLR) (2.5°x2.5°) data provided by the NOAA/OAR/ESRL PSL, Boulder, Colorado, USA., downloaded from https://psl.noaa.gov/data/gridded/data.uninterp_OLR.html. (iii) Daily wind and geopotential height at 200hPa from NCEP/NCAR reanalysis (Kalnay et al., 1996).

3. Results

The important features of rainfall anomalies over India and Indian ocean (Fig. 1) for weak rainfall spells during JJAS 2018 (14-21June (WS1), 27July-7August (WS2), 9-20September (WS3), 24-30 September (WS4)) identified based on the criteria by Rajeevan et.al. (2010) are: (i)There are large differences in rainfall anomaly pattern of four weak spells. WS2 and WS3 are the long intense events. (ii)Rainfall anomaly pattern of WS2 over India closely resemble the composite rainfall anomalies associated with breaks based on (1888–1967) (Ramamurthy, 1969), which is characterized by large negative anomalies over monsoon core zone (MCZ;18°-28°N, 65°-88°E), negative anomalies over west coast, while positive anomalies over northeast India in association with the northward shift of the monsoon trough to the foothills of the Himalaya. WS2 and WS3 pattern are similar over India except for the absence of increased rainfall over the foothills in WS3. (iii)Rainfall anomalies of opposite sign over MCZ and Equatorial Indian Ocean (EIO) in WS4 is indicative of the mutual competition between convection over India and EIO (Sikka and Gadgil,1980). Out-of-phase OLR anomalies over MCZ and Northwest Pacific Ocean (NWPO) (Raman, 1955) are linked with the occurrence of WS1 and WS4 (Fig. 2). A quadrupole structure comprising of positive (negative) OLR anomalies over the Indian region and equatorial west Pacific (EIO and NWPO) (Gadgil and Joseph, 2003) is observed during WS1 and WS4 (Fig. 2). Enhanced convection over foothills of the Himalaya and large parts of tropical Pacific Ocean possibly caused WS2 (Fig. 2). Influence of the intrusion of deep trough in the mid-latitude westerlies into India in the upper troposphere (Ramaswamy,1962) on formation of WS3 is evident (Fig. 3).

References

- Gadgil, S. and Joseph, P.V., 2003. On breaks of the Indian monsoon. Proc. Ind. Aca. Sci. (EPS), 112, 529–558
- Kalnay, E., et al., 1996. The NCEP/NCAR 40-year re-analysis project. Bull. Amer. Meteorol. Soc. 77, 437–471.
- Krishnan R, et al. 2000. Dynamics of breaks in the Indian summer monsoon; J. Atmos. Sci. 57, 9, 1354– 1372.
- Mitra, A.K. et al. 2009. Daily Indian precipitation analysis Formed from a merge of Rain-gauge Data with the TRMM TMPA Satellite-derived rainfall estimates, J. Meteor. Soc. Japan, vol. 87A, 265-279.
- Raman, C. R. V.1955. Breaks in Indian southwest monsoon and typhoons in southwest Pacific. Cur. Sci., 24, 219–220.
- Rajeevan, M, et al. 2010. Active and Break Spells of the Indian Summer Monsoon, J. E. S. S. 119,3, 229–247.
- Ramamurthy, K., 1969. Some aspects of ‘‘break’’ in the Indian southwest monsoon during July and August. Forecasting Manual, IMD publication, FMU, Rep. 4, 18.3.
- Ramaswamy C. 1962. Breaks in the Indian summer monsoon as a phenomenon of interaction between the easterly and the subtropical westerly jet streams. Tellus 14, 337–349
- Sikka D. R., Gadgil, S., 1980. On the maximum cloud zone and the ITCZ over India longitude during the southwest monsoon. Mon. Wea. Rev., 108, 1840–1853.

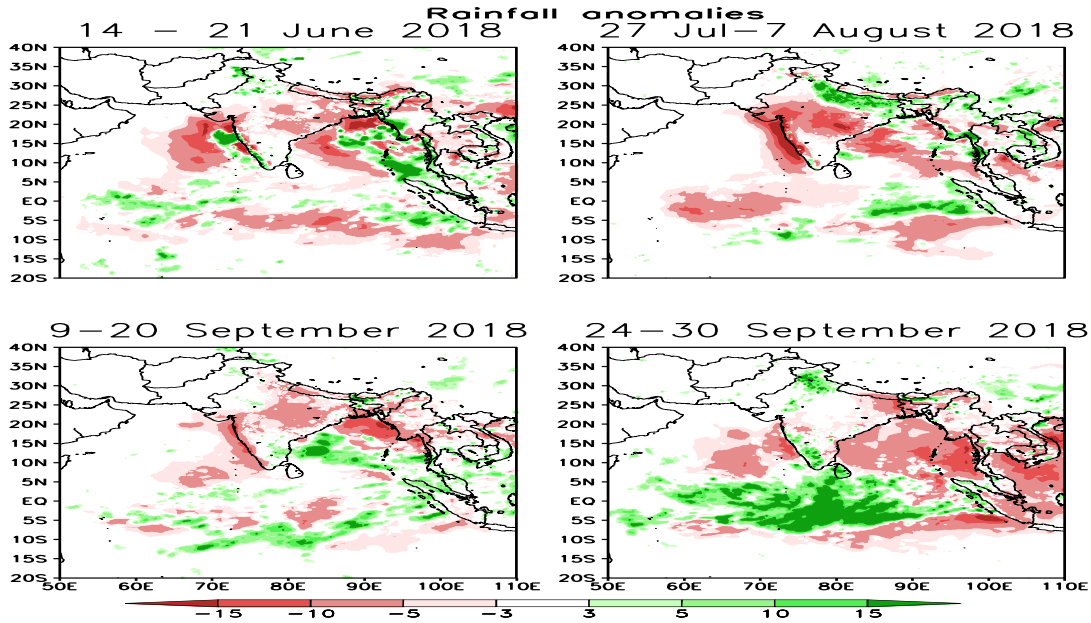

Figure 1: Spatial distribution of rainfall anomalies. Top left (Weak spell 1), top right (weak spell 2), bottom left (weak spell 3), bottom right (weak spell 4)

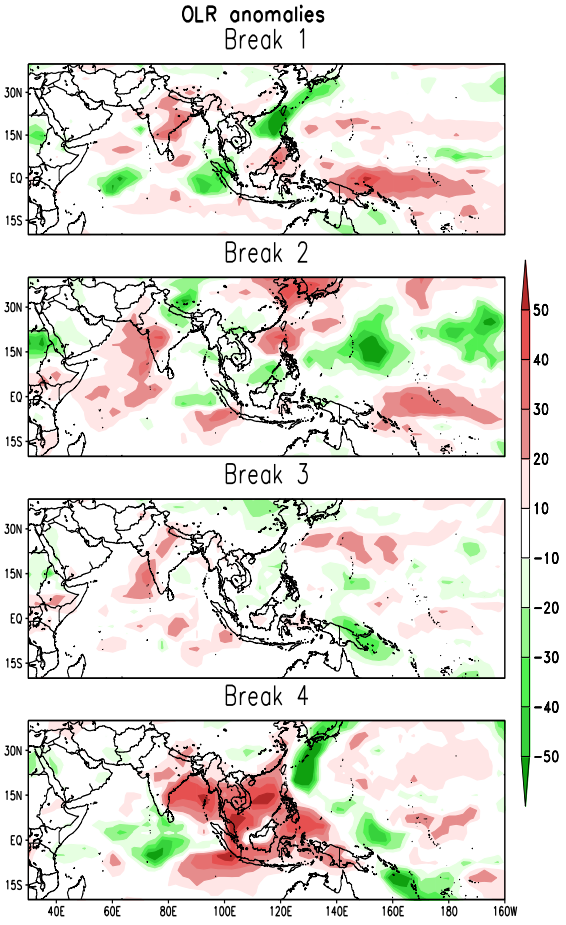

Figure 2: Spatial distribution of OLR anomalies over tropical Indo-Pacific. From top to bottom (weak spell 1, weak spell 2, weak spell 3, weak spell 4) respectively.

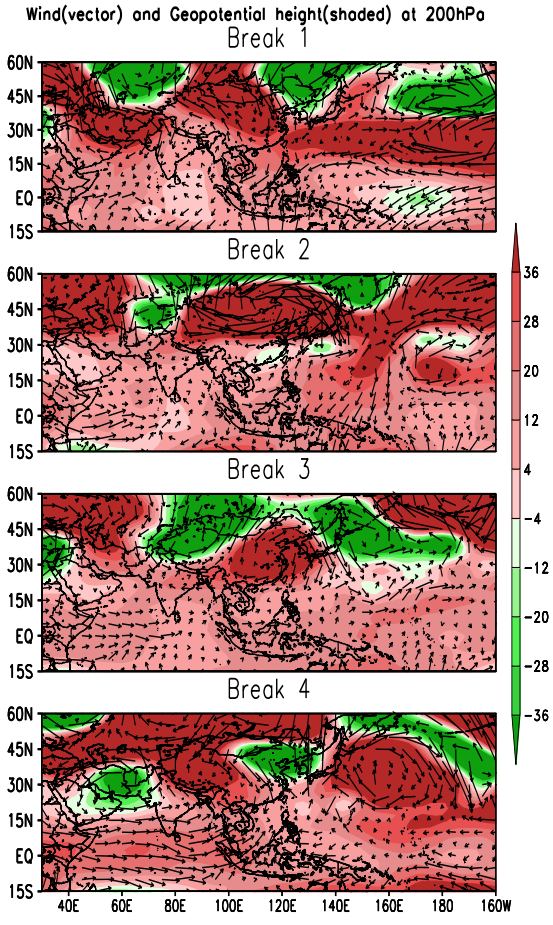

Figure 3: Spatial distribution of Wind (vector) overlaid by Geopotential height at 200hPa (shaded) over tropical Indo-Pacific. From top to bottom (weak spell 1, weak spell 2, weak spell 3, weak spell 4) respectively.

Changes of the El Niño quasi-cyclic dynamics from the analysis of phase portraits

Mokhov I.I.[1,2], Medvedev N.N.[2]

[1]A.M. Obukhov Institute of Atmospheric Physics RAS, Moscow

[2] Lomonosov Moscow State University

mokhov@ifaran.ru

Long-period changes of the El Niño / Southern Oscillation (ENSO) characteristic periods are analyzed with the use of special method of cycles proposed in [1] (see also [2,3]). This method is based on the analysis of phase portraits for quasi-cyclic processes like ENSO. ENSO processes are characterized by the time series of the Southern Oscillation Index (SOI) and sea surface temperature $T(t)$ in the Pacific equatorial basins Niño-3, Niño-3.4 and Niño-4 (https://psl.noaa.gov/gcos_wgsp/). In particular, if there is a statistically significant linear regression of $d^2T(t)/dt^2$ on $T(t)$ with a negative regression coefficient $-\omega^2(t)$, then the process can be fitted by a harmonic oscillator:

$$d^2T/dt^2 + \omega^2 T = 0, \qquad (1)$$

$$T(t) = A(t)sin[\omega(t)t + \varphi(t)]\,. \qquad (2)$$

The variables dT/dt and d^2T/dt^2 can be determined by taking the second-order finite differences of the original time series $T(t)$. The characteristic frequency $\omega(t)$ and corresponding period $P(t)$ are calculated using the least-squares fitting technique at a moving segment of length I_0. To filter out the higher frequency noise, the raw data can be smoothed taking running means at the window I_s.

Figure 1 (a,b) shows phase portraits for ENSO by the data for indices Niño-3 (a) and Niño-4 (b) for the period 1950-2020 (with Is = 12 months). Trajectories for the strongest El Niño events in last decades are highlighted in different colors. Difference between the phase portraits in Fig. 1 indicates a substantial difference in the dynamics of El Niño phenomena of different types, characterized by temperature anomalies in the eastern and central equatorial regions of the Pacific Ocean.

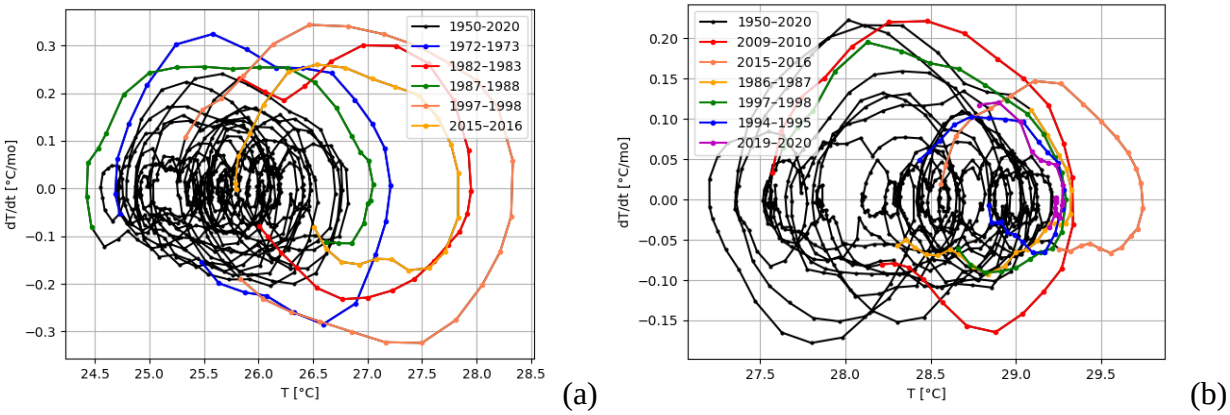

Fig. 1. Phase portraits for ENSO by the data for indices Nino 3 (a) and Nino 4 (b) for the period 1950-2020 (with I_s = 12 months)

Figure 2 (a-d) shows changes of periods of ENSO, characterized by various indices: Niño-3 (a), Niño-4 (b), Niño-3.4 (c), SOI (d) from analysis of data for the period 1870-2020 with I_s = 12 months and I_0 = 120 months. Black curves (corresponding to the 30-years running means)

characterize long-term changes, against the background of which there are significant interdecadal variations.

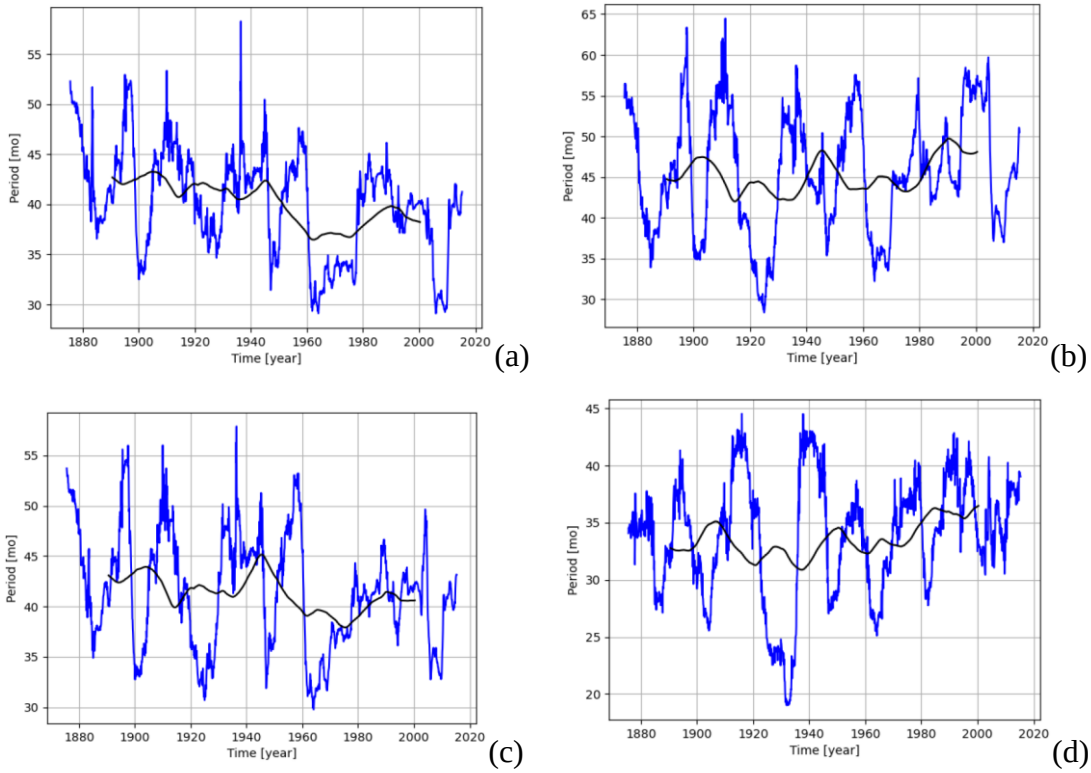

Fig. 2. Changes of periods of ENSO, characterized by various indices: Niño-3 (a), Niño-4 (b), Niño-3.4 (c), SOI (d) from analysis of data for the period 1870-2020 with I_s = 12 months and I_0 = 120 months (black curves correspond to the 30-years running means).

According to the results obtained, changes in the characteristic ENSO periods determined by different indices are very different. In particular, significant differences are associated with changes for Niño-3 and Niño-4 indices, which characterize different manifestations of El Niño in the eastern and central equatorial regions of the Pacific Ocean.

This work was supported by the Russian Science Foundation (project 19-17-00240).

References

[1] Mokhov I.I. (1993) Climate changes: Analyses of global cycles. *Ann. Geophys.* **12** (Suppl. II): C334.

[2] Mokhov I.I., Eliseev A.V., Khvorostyanov D.V. Evolution of the characteristics of interannual climate variability associated with the El Niño and La Niña phenomenon. *Izvestiya Atmos. Ocean. Phys.* **36**: 681–690, 2000

[3] Mokhov I.I., Khvorostyanov D.V., Eliseev A.V. (2004) Decadal and longer term changes in El Nino – Southern Oscillation characteristics. *Intern. J. Climatol.* **24**: 401- 414.

Integral index of blocking activity in the atmosphere of Northern Hemisphere during last decades

Mokhov I.I.[1,2], Timazhev A.V.[1]

[1]A.M. Obukhov Institute of Atmospheric Physics RAS, Moscow

[2] Lomonosov Moscow State University

mokhov@ifaran.ru

To characterize total activity of atmospheric blockings over extended areas and concrete time intervals (for instance: over the territory of Russia as a whole during vegetation period) an integral blocking index I_I was proposed using local diagnostics of atmospheric blockings in each longitudinal sector with $\Delta\lambda = 2.5°$. In particular, in [1], a variant of the integral index of blocking activity I_I was used when analyzing fire hazardous seasons for a specific time interval Δt from April to October in the Russian longitudinal sector 20°-180°E. The I_I value was determined by the percentage of the sum of days with diagnosed atmospheric blocking in all local sectors $\Delta\lambda$ of the Russian longitudinal sector to the maximum possible number of days with atmospheric blockings. The criterion proposed in [2] was used as a local blocking condition with the necessary condition for its fulfillment for at least 5 consecutive days.

Here, we present estimates of the integral blocking index for the Northern Hemisphere (NH) and for Russia as a whole based on the ERA-Interim reanalysis data for the 40-year period 1979–2018 with a two-dimensional (2D) local blocking condition according to [3].

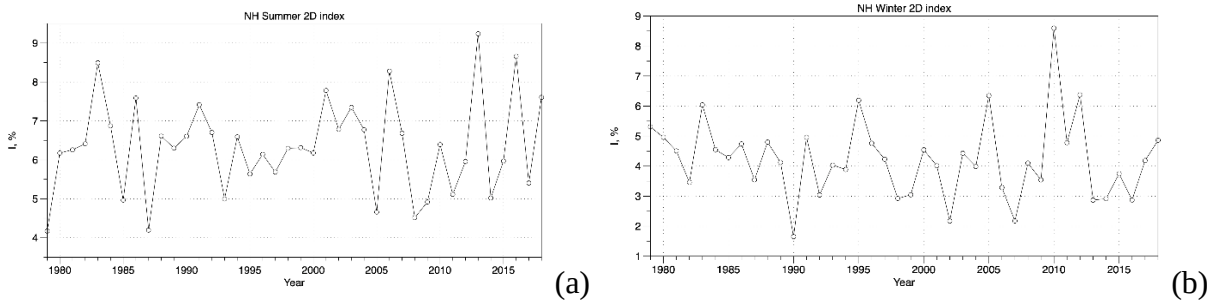

(a) (b)

Fig. 1. Interannual variations of I_I for the NH as a whole for the summer (a) and winter (b) seasons.

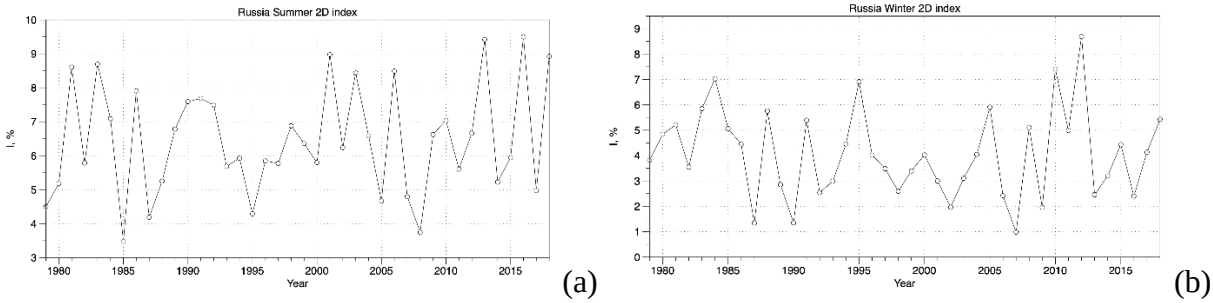

(a) (b)

Fig. 2. Interannual variations of I_I for Russia as a whole for the summer (a) and winter (b) seasons.

Figures 1,2 show the interannual variations of I_I for the NH (Fig. 1) and for Russia as a whole (Fig. 2) for the summer (a) and winter (b) seasons. Table 1 shows annual and seasonal estimates of integral index of blocking activity I_I [%] in the Northern Hemisphere and Russia for two periods (1979-1998 and 1999-2018).

Table 1. Annual and seasonal integral index of blocking activity (%) in the Northern Hemisphere and Russia for two periods (1979-1998 and 1999-2018).

Region	Season	1979-1998 Mean Value (%) (±Standard Deviation)	1999-2018 Mean Value (%) (±Standard Deviation)
Northern Hemisphere	Annual	4.6 (±0.6)	4.6 (±0.6)
	Winter	4.3 (±1.1)	4.1 (±1.6)
	Spring	4.3 (±1.1)	4.1 (±1.0)
	Summer	6.2 (±1.1)	6.5 (±1.7)
	Autumn	3.4 (±0.9)	3.5 (±1.0)
Russia	Annual	4.2 (±0.8)	4.2 (±0.8)
	Winter	4.2 (±1.6)	4.0 (±1.9)
	Spring	3.6 (±1.2)	3.2 (±1.1)
	Summer	6.2 (±1.5)	6.7 (±1.7)
	Autumn	2.7 (±1.3)	3.0 (±1.3)

The estimates indicate a large interannual variability of I_I in all seasons for the NH as a whole and for different regions, including Russia as a whole. The highest average values of I_I were obtained for summer, while the lowest ones were estimated for autumn. Comparison of results for two 20-year periods in Table 1 shows relatively small changes of the I_I mean values, especially of the annual-mean values. Remarkable increase of the I_I standard deviations was obtained for the NH for Russia as a whole in summer and in winter.

This work was supported by the Russian Science Foundation project 19-17-00240.

References

[1] Mokhov I.I., Sitnov S.A., Tsidilina M.N., Voronova O.S. (2021) NO_2 emission into the atmosphere from forest fires in Russia in relation with atmospheric blocking events. *Atmos. Ocean. Optics* **34** (6): 1-5. (in Russian)
[2] Tibaldi S., Molteni F. (1990) On the operational predictability of blocking. *Tellus* **42A**: 343-365.
[3] Scherrer S., Croci-Maspoli M., Schwierz C., Appenzeller C. (2006) Two-dimensional indices of atmospheric blocking and their statistical relationship with winter climate patterns in the Euro-Atlantic region. *Intern. J. Climatol.* **26**: 233-249.

Sensitivity of the surface air temperature in different NH latitudes to changes in anthropogenic forcing and natural climate modes

Mokhov I.I.[1,2], Smirnov D.A.[3]

[1]A.M. Obukhov Institute of Atmospheric Physics RAS, Moscow, mokhov@ifaran.ru
[2]Lomonosov Moscow State University, Moscow
[3]Saratov Branch of V.A. Kotel'nikov Institute of RadioEngineering and Electronics RAS, Saratov, smirnovda@yandex.ru

Estimates of the sensitivity of the surface air temperature in different latitudinal belts of the Northern Hemisphere (NH) to the radiative forcing of greenhouse gases (GHG) and changes in the modes of natural climatic variability, including the Atlantic Multidecadal Oscillation (AMO) and El-Nino / Southern Oscillation (ENSO), have been obtained similarly to [1-3] (see also [4,5]). Three-component autoregressive (AR) models were used for surface temperature anomalies T with a year lag:

$$T_n = a_0 + a_1 T_{n\text{-}1} + a_2 I_{GHG,\text{n-}1} + a_3 I_{m,\text{n-}1} + \xi_n. \qquad (1)$$

Here n is the discrete time (years), ξ_n is the noise (residual model errors), I_{GHG} is the radiative forcing of greenhouse gases, a_0, a_2, and a_3 are the model coefficients, $I_{m,\text{n-}1}$ is the climate mode index (AMO or ENSO).

Table 1. The coefficients (with the doubled standard deviations Δ) of empirical models (1) for different latitudinal belts in the Northern Hemisphere.

Northern Hemisphere degrees of latitude	Coefficients of empirical models (1)			
	AMO		ENSO	
	$a_2 \pm \Delta a_2$ $K \cdot W^{-1} \cdot m^2$	$a_3 \pm \Delta a_3$	$a_2 \pm \Delta a_2$ $K \cdot W^{-1} \cdot m^2$	$a_3 \pm \Delta a_3$
60 – 90	0.35±0.10	0.70±0.50	0.30±0.10	0.09±0.12
30–60	0.21±0.06	0.44±0.25	0.16±0.05	0.03±0.05
0 – 30	0.15±0.05	0.23±0.20	0.14±0.05	0.04±0.05

The estimates of the coefficients of the model (1) characterizing the sensitivity of temperature anomalies in different latitudinal belts to changes of I_{GHG} and I_m for the period 1880-2012 are given in Table 1. The analysis used annual long-term data for surface temperature for different latitudinal belts (ftp://ftp.ncdc.noaa.gov/pub/data/). To characterize the key modes of natural climatic variability, we used the AMO index (http://www.esrl.noaa.gov/psd/data/) and ENSO index Nino 3.4 (http://www.esrl.noaa.gov/psd/data/).

Estimates of the coefficients in Table 1 are statistically significant at the 95% level if they exceed the doubled standard deviation. According to them, the temperature sensitivity to the GHG radiative forcing in Arctic latitudes is more than twice as large as that in the tropical latitudes, both when accounting for AMO and for ENSO. The errors in the estimates of the sensitivity coefficients in Arctic latitudes are twice as large as in the tropical ones.

The estimates of temperature sensitivity to changes in AMO and ENSO indices are generally less significant than to changes in GHG radiative forcing. Estimates of the temperature sensitivity to AMO changes are more significant than those to ENSO changes in all latitudinal belts of the NH. The temperature sensitivity to changes in AMO and ENSO indices is greatest in the Arctic latitudes. The corresponding errors in the estimates of the temperature sensitivity are greatest in Arctic latitudes. The temperature sensitivity to changes in the AMO index in Arctic latitudes is three times higher than that in the tropical latitudes, and more than one and a half times higher than that in the middle latitudes. The estimates of the temperature sensitivity and their errors in Arctic latitudes to changes in the ENSO index are more than twice as large as those in the tropical and middle latitudes.

This work was supported by the Russian Science Foundation (project 19-17-00240).

References

[1] Smirnov D.A, Mokhov I.I. (2009) From Granger causality to “long-term causality”: application to climatic data *Phys. Rev. E***80** (1): 016208

[2] Smirnov D.A, Mokhov I.I. (2015) Relating Granger causality to long-term causal effects *Phys. Rev. E***92** (4): 042138.

[3] Mokhov I.I., Smirnov D.A. (2020) Estimates of the contribution of key natural modes and anthropogenic forcing to global surface temperature trend at different temporal horizons. *Research Activities in Earth System Modelling.* E. Astakhova (ed.).WCRP Rep. No.6/2020: 2.11-2.12.

[4] Mokhov I.I., Smirnov D.A. (2018) Estimating the contributions of the Atlantic Multidecadal Oscillation and variations in the atmospheric concentration of greenhouse gases to surface air temperature trends from observations. *Doklady Earth Sci.***480** (1): 602–606.

[5] Mokhov I.I., Smirnov D.A. (2018) Contribution of greenhouse gas radiative forcing and Atlantic Multidecadal Oscillation to surface air temperature trends. *Russ. Meteorol. Hydrol*. **43** (9): 557–564.

Polar mesocyclones and their variability from STARS data

Poroshenko A.G.[1], Akperov M.G.[2], Mokhov I.I.[1,2]

[1]Lomonosov Moscow State University

[2]A.M. Obukhov Institute of Atmospheric Physics RAS

poroshenko.ag18@physics.msu.ru

The annual variations of the frequency of occurrence of polar lows (PL) and their distribution functions depending on the lifetime and characteristic size are characterized according to STARS (Sea Surface Temperature and Altimeter Synergy for Improved Forecasting of Polar Lows) data for the period 2002-2010 [1] (see also [2]). The STARS data are based on satellite infrared images obtained using the AVHRR (Advanced Very-High-Resolution Radiometer) instrument and characterize the parameters of polar mesocyclones over the waters of the Norwegian and Barents Seas with hourly resolution.

Figure 1 characterizes the average number of PL for different months of the year according to STARS data (2002-2010). According to the analyzed data, PL are most often observed in March and January, more than 3 cyclones per month on average. The maximum interannual variability with a standard deviation of more than 2 cyclones is observed in March. In January, the process of PL formation is more stable, with a standard deviation of about 1 cyclone. By the beginning of summer, the probability of PL formation decreases to zero and increases at the beginning of the fall season, reaching its local maximum in November (about 2 cyclones per month). One should note the instability of the manifestation of the local maximum in November, i.e., the interannual variability is large.

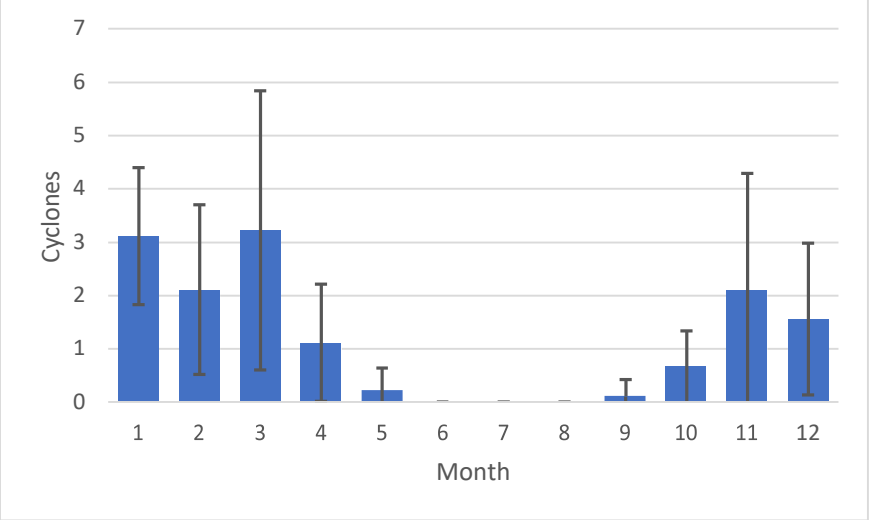

Fig. 1. The average number of PL for different months of the year according to STARS data. Standard deviations are shown by vertical lines.

Figure 2 shows estimates of the probability of PL according to the STARS data, depending on their characteristic size. According to Fig. 2, the PLs with a characteristic size of about 200 km are the most likely.

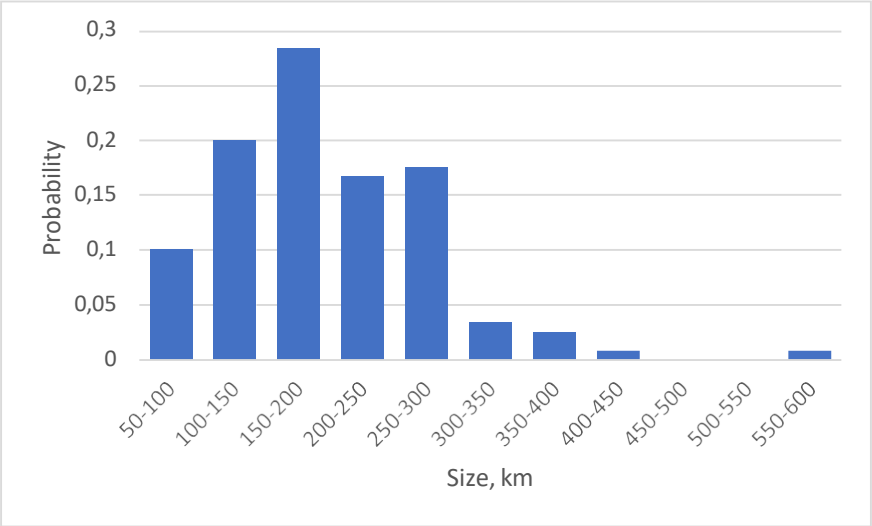

Fig. 2. The estimates of the PL probability depending on their characteristic size R (according to STARS data).

Figure 3 presents estimates of the probability of PLs according to STARS data depending on their characteristic size. According to Fig. 3, short-lived PLs with a lifetime of no more than 12 hours are the most likely.

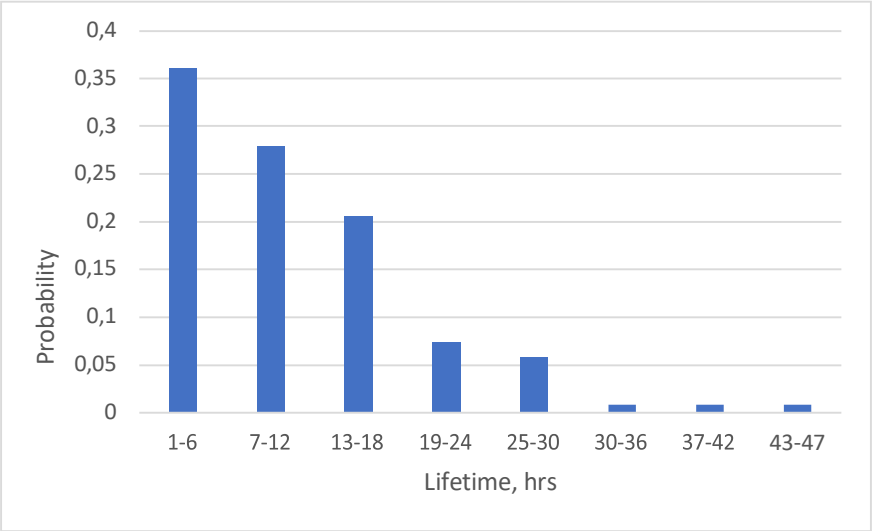

Fig. 3. Estimates of the PL probability depending on their lifetime (according to STARS data).

The features of the lifetime and characteristic dimensions of PLs for different months of the year are manifested. In particular, the biggest values of the average duration were noted for March and January - about 1.5-2 days. For the other months, the average PL duration is less than a day (including November, when the local maximum of the average lifetime appears).

The analysis of PLs was carried out within the framework of the RSF project (19-17-00240).

References

[1] Noer G., Saetra Ø., Lien T., Gusdal Y. (2011) A climatological study of polar lows in the Nordic Seas. *Q. J. R. Meteorol. Soc.* **137**: 1762–1772.
[2] Akperov M.G., Mokhov I.I., Dembitskaya M.A. (2017) Arctic mesocyclones from satellite data and model simulations. Current Problems in Remote Sensing of the Earth from Space. **14** (3): 207-304. DOI:10.21046/2070-7401-2017-14-3-297-304

Relation of Eurasian snow with regional India summer monsoon rainfall

Amita Prabhu [1,*] and Sujata K. Mandke [1]
[1] Indian Institute of Tropical Meteorology, Ministry of Earth Sciences, India
*amitaprabhu@tropmet.res.in, amin@tropmet.res.in

1. Introduction

Relationship of preceding winter/spring Eurasian snow with the Indian summer monsoon rainfall has been widely recognized. However, previous studies have tended to mainly focus on the snow-monsoon teleconnection using all-India averaged summer monsoon rainfall index (AISMR) (Bamzai and Shukla, 1999; Zhang et al., 2019), while devoting less effort to examining the regional features over India. Some of the earlier investigations that examined the spatial distribution of Indian rainfall association with antecedent Eurasian snow (Parthasarathy and Yang, 1995; Fasullo, 2004) were constrained by the coarse spatial resolution of rainfall data over India. Snow-monsoon relationships are complex due to the significant spatio-temporal variations of both snow (Bamzai and Shukla, 1999) and monsoon (Hrudya et. al. 2021). As a result, AISMR index is not appropriate to delineate the specific regions over India that are responsible for the well-known snow-monsoon relation. Recent multiple high-resolution gridded rainfall datasets along with the reanalysis datasets, provide prospects to appraise regional aspects of snow-monsoon link over India. In the present study, we attempt to answer a question- Do European Centre for Medium-Range Weather Forecasts ERA5 reanalysis data capture the spatial characteristics of snow-monsoon relation over India?

2. Data

Reanalysis: (i) Monthly rainfall and snow water equivalent (SWE) for the period 1980–2007 are obtained from the ERA5 reanalysis dataset at 0.25° spatial resolution (Hersbach et al. 2020). Observation: (i) Daily rainfall grid point data developed by India Meteorological Department (IMD) across the Indian landmass (Pai et al., 2014), (ii)National Snow and Ice Data Center (NSIDC) archived SWE data from Scanning Multi-channel Microwave Radiometer (SMMR) and Special Sensor Microwave/Imager (SSM/I) for the period November 1980-2007. This dataset has been enhanced using snow cover frequencies, and is gridded to the Northern and Southern 25km Equal-Area Scalable Earth Grids (Armstrong et al., 2002). SWE is hereafter referred to as snow.

3. Results

The analysis in the study is conducted for 1980-2007 due to availability of NSIDC SWE data for this period. The seasonal averages are defined as: December to March of the following year (DJFM) as winter season, April-May (AM) as spring season and June-September (JJAS) as summer monsoon season. Correlation coefficient (CC) between snow averaged over Eurasian domain (50- 70°N; 20-140°E) and the ensuing summer monsoon season rainfall at each grid point over India using ERA5 and corresponding observed data (OBS) is illustrated, both for winter (Fig.1a-b) and spring (Fig.1c-d) snow respectively. CC between snow and rainfall over India (Fig.1) is hereafter referred to as snow-monsoon relation. Winter snow-monsoon relation (OBS) (Fig.1b) is characterized by a 'Negative-Positive-Negative' (NPN) tri-polar spatial structure demonstrated as significant negative CC over the northern and south-western regions of India as well as over the parts of peninsular India, whereas positive CC is observed over east-central India. Spring snow-monsoon (OBS) relation (Fig.1d) is substantially weak and also the regional features vary from winter snow-monsoon (OBS) relation (Fig.1b). The tri-polar pattern of winter snow-monsoon (OBS) (Fig. 1b) relation is captured in ERA5 (Fig.1a), although regions with significant CCs and their spatial extent in ERA5 markedly deviates from that of corresponding observation. Although the spring snow-monsoon (OBS) relation (Fig.1d) is substantially weak, it is robust in ERA5 (Fig.1c) with tri-polar spatial pattern consistent with the winter snow-monsoon (ERA5) relation (Fig.1a).

References

- Armstrong, R.L., Brodzik, M.J., 2002. Hemispheric-scale Comparison and Evaluation of Passive Microwave Snow Algorithms. Ann. Glaciol. 34, 38-44.
- Bamzai A. S., and Shukla, J., 1999. Relation between Eurasian snow cover, snow depth, and the Indian summer monsoon: An observational study. J. Climate, 12, 3117–3132.
- Fasullo, J., 2004. A stratified diagnosis of the Indian monsoon–Eurasian snow cover relationship. J. Clim. 17, 1110–1122.
- Hersbach, H. et al., 2020. The ERA5 global reanalysis. Q. J. R. Meteoro. Soc. 146, 1999–2049.
- Hrudya, P.H., Varikoden, H., Vishnu, R., 2021. A review on the Indian summer monsoon rainfall, variability and its association with ENSO and IOD. Met. and Atmos. Phy. 133,1–14
- Pai DS. et al., 2014. Development of a new high spatial resolution (0.25 × 0.25 degree) long period (1901– 2010) daily gridded rainfall data set over India and its comparison with existing data sets over the region. Mausam 65(1),1–18.
- Parthasarathy, B., Yang, S., 1995. Relationships between regional Indian summer monsoon rainfall and Eurasian snow cover. Adv. Atmos. Sci. 12, 143–150.
- Zhang, T. Wang, G. et al., 2019. The weakening relationship between Eurasian spring snow cover and Indian summer monsoon rainfall. Sci. Adv. 5, eaau8932.

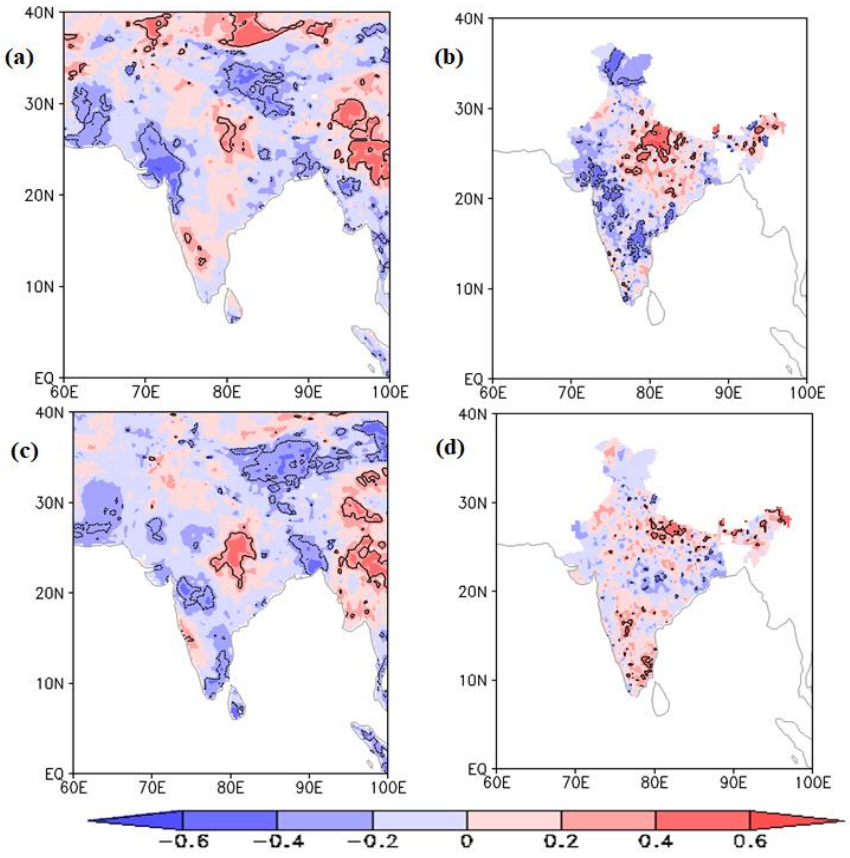

Figure 1: (a) Correlation coefficient (shaded) of ERA5 summer monsoon (JJAS) rainfall at each grid point over India and neighbourhood with the preceding winter (DJFM) snow averaged over the region of Eurasia [20°-140°E, 50°-70°N], based on 1980-2007.
(b) Same as (a) except with IMD observed rainfall data at each grid point over Indian main land and satellite snow (NSIDC) data.
(c) Same as (a) except with preceding spring (AM) snow.
(d) Same as (b) except with preceding spring (AM) snow.
Black solid contours represent significance at 95% confidence level.

A comparison of deep convection detection algorithms based on thresholding techniques applied to Meteosat-11 satellite data for European Russia

Shishov A.E.
The Hydrometcentre of Russia, 123376 Moscow, Russia, B. Predtechensky per.
shandruha@gmail.com

Data from the infrared channels of the Spinning Enhanced Visible and Infrared Imager (SEVIRI) provides a convenient satellite way of detecting and analyzing deep convective clouds during both daytime and nighttime. It is the primary instrument of the geostationary satellite Meteosat-11, which has a sampling distance of 3-5 km depending on the longitude and latitude of the observed area, and a temporal resolution of 15 min. Motivated by the problem of forecasting hazards for aviation, this study presents a comparison of four different detection algorithms designed to detect deep convective clouds, which will be referred to as convective objects (COs).

The quality of each algorithm is evaluated on data for the period July 14-16, 2020. The analysis was conducted using the measurements of brightness temperature in the following infrared window channels: 10.8 μm - $T_{10.8}$, 6.2 μm – $T_{6.2}$, 7.3 μm – $T_{7.3}$. The region of interest was confined between 30° and 70° latitude, 20° and 75° longitude. The dataset consisted of 288 observations, each one being a set of three images (one image per channel).

Algorithm 1. Thresholding criteria included critical brightness temperature values - that is, pixels with brightness temperature $T_{10.8}$ below 233 K as well as temperature differences ($T_{6.2} - T_{10.8}$) and ($T_{6.2} - T_{7.3}$) above -10 and -4 K correspondingly were selected [1]. Furthermore, since the shape of deep convective cloud boundary as viewed from outer space is typically convex [2], we also used an additional convexity criterion based on solidity index [3]: the ratio of CO area to the area of its convex hull must be above 0.7.

Algorithm 2. Assuming that the temperature of a deep convective cloud top is at least as low as 220 K [4], we added one more criterion to the ones mentioned before: a candidate object must have at least one pixel with brightness temperature $T_{10.8}$ below 220 K in order to be considered a CO.

Algorithm 3. The previous algorithm was augmented with the variable thresholding technique applied to IR 10.8 channel: if a candidate object did not meet the convexity criterion mentioned above, the critical value was iteratively lowered (which caused the object to shrink in size and change in shape) until it did or until a maximum number of iterations was reached.

Algorithm 4. An approach proposed by K.M. Bedka [5]. It takes into account not only the brightness temperature $T_{10.8}$ at a given pixel, but also the mean of its neighbours and standard deviation from that mean.

The detections were validated using the distributions of two parameters: CO lifetime defined as the number of successive steps at which the same CO was detected (converted to time in minutes through multiplication by 15); and CO maximum area defined as the maximum size in km^2 reached by that CO during its lifetime (see Table 1). The analysis revealed that Algorithm 1 detected a large number of small short-lived COs, i.e. those with lifetimes less than one hour and areas less than 310 km^2. Hence, it is applicable to the task of detecting weak convection as it occurs frequently under unstable atmospheric conditions. In the meanwhile, the stricter criteria of Algorithm 2 enabled it to detect significantly fewer small short-lived COs, since the tops of the most of them were warmer than the defined threshold of 220 K. As a result, the detected objects were more powerful, had a bigger size and a longer lifetime. COs detected by Algorithm 3 were more numerous due to the variable thresholding technique, which increased the chances of an object to meet the convexity criterion. Algorithm 4 distinguished itself by the greatest number of detected COs of all sizes and lifetimes. It can extract valuable information from IR 10.8 channel alone as it considers spatial brightness temperature gradients. However, among the detected COs there were too many small objects that lived for less than one hour as well as some big ones with distorted contours (see Figure 1). Given that images studied by Bedka had a higher resolution, we conclude that this algorithm requires calibration to yield adequate results on our data.

This research was carried out as part of a collaborative project between Russia and Belarus.

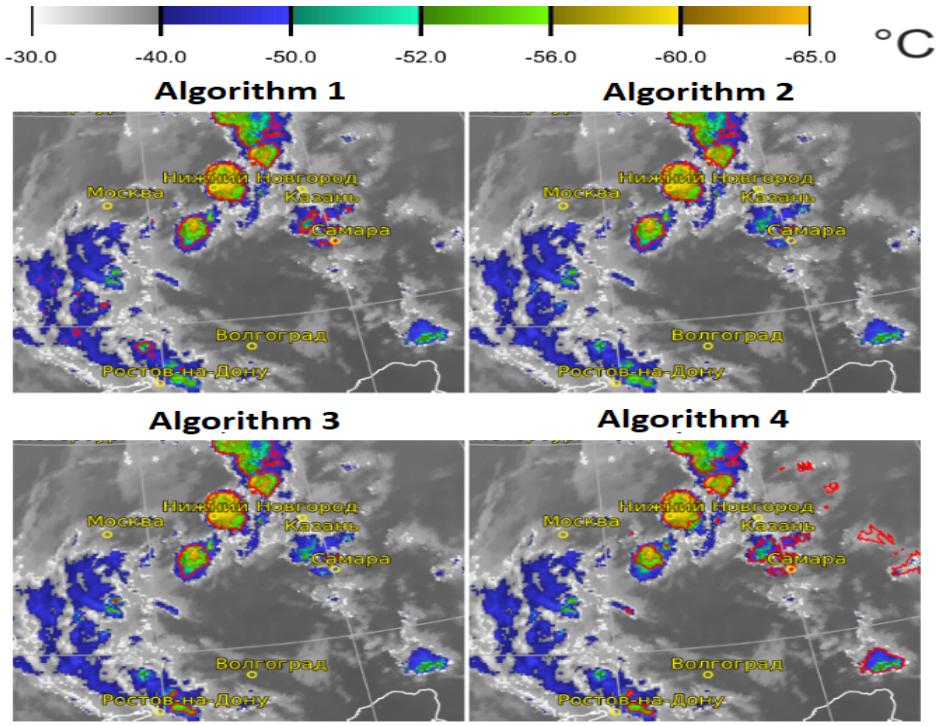

Figure 1. Examples of contours (in red) of COs detected by the algorithms, color-enhanced IR 10.8 channel data as a background, UTC 00:00 2020-07-14

Table 1. Frequency of COs detected by the algorithms, grouped by lifetime and area

Area (km^2)	Lifetime (hours)	Algorithm 1	Algorithm 2	Algorithm 3	Algorithm 4
25-80	< 1	7492	415	1103	11151
	1-6	10	1	2	9
80-310	< 1	2217	108	263	5642
	1-6	3	1	1	89
310-700	< 1	729	77	222	1891
	1-6	9	6	8	110
	6-12	0	0	0	1
700-100000	< 1	540	195	260	1110
	1-6	84	37	58	369
	6-12	4	4	5	34
	12+	0	0	0	4
100000-200000	6-12	1	1	0	0
	12+	0	0	1	0

References

1. Silva Neto C.P. da, Barbosa H.A. A method for convective storm detection using satellite data // Atmósfera. – 2016. – Vol. 29. – № 4. – P. 343-358.
2. Machado L., Desbois M. Structural characteristics of deep convective systems over tropical Africa and the Atlantic ocean // Monthly Weather Review. – 1992. – Vol. 120.
3. Yang M., Kpalma K. A survey of shape feature extraction techniques. – 2007. – Vol. 15.
4. Futyan J., Delgenio A. Deep convective system evolution over Africa and the tropical Atlantic // J. Clim. – 2007. – Vol. 20.
5. Bedka K., Khlopenkov K. A probabilistic multispectral pattern recognition method for detection of overshooting cloud tops using passive satellite imager observations // Journal of Applied Meteorology and Climatology. – 2016. – Vol. 55. – P. 1983-2005.

Heat and cold waves formation in association with atmospheric blockings in the Northern Hemisphere

Timazhev A.V.[1], Mokhov I.I.[1,2]

[1]A.M. Obukhov Institute of Atmospheric Physics RAS, Moscow

[2] Lomonosov Moscow State University

timazhev@ifaran.ru

To characterize the influence of atmospheric blockings in formation mechanism of heat and cold waves a joint analysis of atmospheric blockings and heat/cold waves was carried out for the Northern Hemisphere basing on ERA-Interim reanalysis data for the period 1979–2019. Heat (for summer season) and cold (for winter season) waves were detected using the criterion proposed in [1], with the necessary condition for its fulfillment for at least 3 consecutive days and for the area at least 6×10^5 km^2. The criterion proposed in [2] was used as a local blocking condition in this work, with the necessary condition for its fulfillment for at least 5 consecutive days. Blockings and heat (cold) waves were considered to be associated if the distance between centers of blocking and heat/cold wave was less than 15° of longitude and blocking and heat/cold wave took place at the same time.

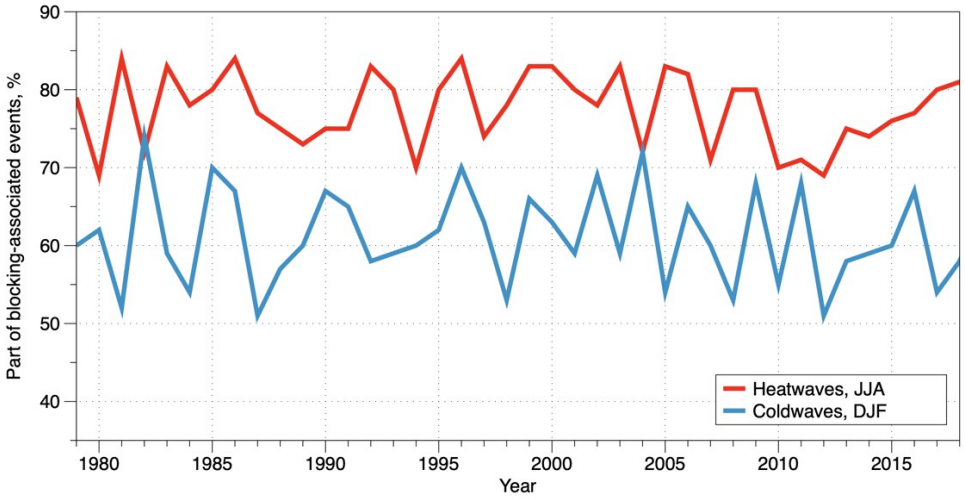

Figure 1. Interannual variations of the fraction (%) of heat and cold waves associated with blocking events.

Figure 1 and Table 1 show the fraction of heat (cold) waves associated with blockings during the 1979– 2019 period in the Northern Hemisphere and two sectors: 0°–30°E and 30°–60°E (only in Table 1). The estimates obtained show that on average about 80% of summer heat waves are associated with blockings. In winter on average about 60% of cold waves are associated with blockings.

Table 1. Number of total and blocking-associated heat and cold waves in the Northern Hemisphere and sectors 0°–30°E and 30°–60°E for the period 1979–2019.

	Heat waves, Summer			Cold waves, Winter		
Number of events	NH	0–30E	30–60E	NH	0–30E	30–60E
With blockings	59	15	16	41	11	13
Total	76	20	22	68	17	24
Part of blocking-associated events	78%	75%	72%	60%	65%	54%

Figure 2 shows the intensity of blocking-associated summer heat waves in dependence on blocking duration in the Northern Hemisphere and two sectors (0°–30°E and 30°–60°E) for the period 1979–2019.

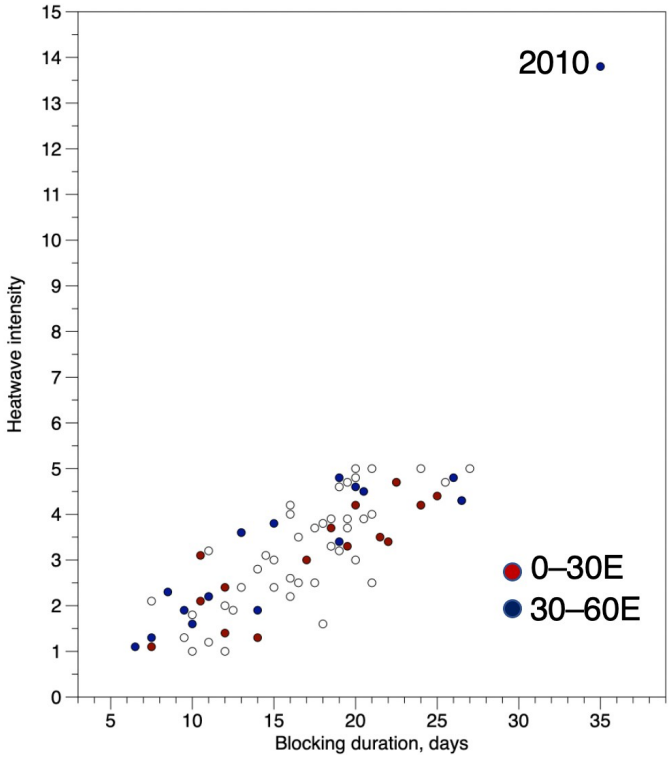

Figure 2. Intensity of blocking-associated summer heat waves in dependence on blocking duration in the Northern Hemisphere and sectors 0°–30°E and 30°–60°E for the period 1979–2019.

According to Fig. 2 the relationship between the duration of blockings and the intensity of the heat wave in the period 1979–2019 did not change significantly, except for the case of a record blocking duration and record heat wave intensity in the summer of 2010 in the European part of Russia.

This study was supported by the Russian Science Foundation (project no. 19-17-00240).

References

[1] Perkins S.E., Alexander L.V. (2013). On the measurement of heat waves. *J. Climate*. **26**(13): 4500–4517.
[2] Tibaldi S., Molteni F. (1990) On the operational predictability of blocking. *Tellus* **42A**: 343–365.